Structural and Magnetic Study of O₂ Molecules Arranged along a Channel in a Flexible Single-Crystal Host Family

Satoshi Takamizawa,*,†,‡ Ei-ichi Nakata,† Takamasa Akatsuka,†
Chihiro Kachi-Terajima,† and Ryosuke Miyake†

*International Graduate School of Arts and Sciences, Yokohama City University, 22-2 Seto,
Kanazawa-ku, Yokohama 236-0027, Japan, and PRESTO, Japan Science and Technology
Agency (JST), Honcho, Kawaguchi, Saitama 332-0012, Japan*

Received August 8, 2008; E-mail: staka@yokohama-cu.ac.jp

Abstract: We report the magnetic behaviors of O₂ molecules, which aligned in the channels of four types of single-crystal adsorbents, [M₂(bza)₄(pyz)]ₙ (bza = benzoate; pyz = pyrazine; M = Rh^{II} (**1a**) and Cu^{II} (**1b**)) and [M₂(bza)₄(2-mpyz)]ₙ (2-mpyz = 2-methylpyrazine; M = Rh^{II} (**2a**) and Cu^{II} (**2b**)). The X-ray single-crystal structures at various temperatures from 10 to 298 K were determined for O₂-included crystals of **1a** and **2a**. All adsorbed O₂ molecules exhibited abnormal magnetic phases above 4 T in the temperature range around 55−105 K. The magnetic behaviors of adsorbed O₂ molecules between four inclusions were discussed. The existence of the metastable state, which was also suggested by hysteresis on the *M*−*H* curves, was revealed by analysis of the time course of the magnetization. Considering that the abnormal magnetic behavior occurred at relatively high temperatures and a low magnetic field, it was suggested that these behaviors were induced because of the changes of magnetic interaction of included O₂ aggregates involving transformation which is supported by the surrounding of the channels of the single-crystal hosts under the applied magnetic field.

Introduction

It is well-known that oxygen is a simple paramagnetic molecule with a spin $S = 1$ in the ground state, so the magnetism of O₂ has been widely investigated. In the bulk solid state, the phases that can be transformed depending on temperature and pressure have been established by correlation between crystal structure and intermolecular magnetic interaction.[1] Control of the arrangement of such paramagnetic small molecules has been an attractive subject for the study of low-dimensional physico-chemical properties. The specific magnetic state differing from bulk O₂ can be generated by modifying the molecular aggregate structure. Gas adsorption would be an effective approach for controlling the configuration of the light guests. The layered O₂ crystals that form on the graphite surface have been widely investigated crystallographically and magnetically.[2,3] In these phases, it is known that the magnetic interaction mediated by the graphite surface cannot be neglected because of the magnetic interaction between the adsorbed O₂ molecules due to the surface conductivity.[4] Hexagonal boron nitride is also a good candidate for generating uniform O₂ alignment on the surface because this material is an insulator that will not affect the O₂ phases. However, no well-defined crystal structure has been obtained.[5] The magnetic property of adsorbed O₂ molecules in micropores
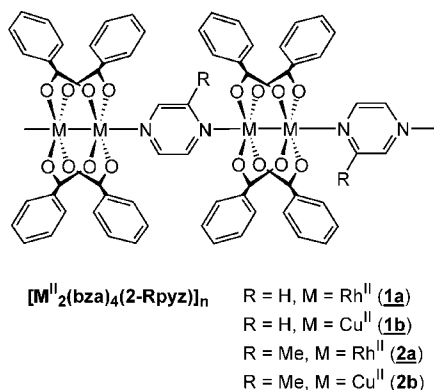
also studied in zeolite[6a] and the activated carbon fibers.[6b] The generated phases were identified by their magnetic behavior rather than by crystallography because they are, unfortunately, not crystalline aggregates.[6] On the other hand, microporous crystals consisting of metal complexes[7] have the possibility to serve as a field for the observation of crystalline aggregates because of their adsorption properties.[8,9] Mori et al. first reported that the magnetic properties of adsorbed O₂ molecules differed

† Yokohama City University.
‡ PRESTO, Japan Science and Technology Agency (JST).
(1) Uyeda, C.; Sugiyama, K.; Date, M. *J. Phys. Soc. Jpn.* **1985**, *54*, 1107.
(2) Köbler, U.; Marx, R. *Phys. Rev. B* **1987**, *35*, 9809.
(3) Steele, W. *Chem. Rev.* **1993**, *93*, 2355.
(4) Murakami, Y.; Suematsu, H. *Phys. Rev. B* **1996**, *54*, 4146.
(5) Shibata, T.; Murakami, Y.; Watanuki, T.; Suematsu, H. *Surf. Sci.* **1998**, *405*, 153.

(6) (a) Takaishi, T.; Yusa, A.; Ogino, Y.; Ozawa, S. *Proc. Int Conf. Solid Surf. 2nd* **1974**, 279. (b) Kanoh, H.; Kaneko, K. *J. Phys. Chem.* **1996**, *100*, 755.
(7) (a) For a review, see: Braga, D.; Grepioni, F. *Top. Cur. Chem.* **2005**, *254*, 71. (b) Albrecht, M.; Lutz, M.; Speck, A. L.; van Koten, G. *Nature* **2000**, *406*, 970. (c) Langeley, P. J.; Hullinger, J. *Chem. Soc. Rev.* **1999**, *28*, 279. For a recent example, see: (d) Papaefstathiou, G. S.; Friscic, T.; MacGillivary, L. R. *J. Am. Chem. Soc.* **2005**, *127*, 14160. (e) Chong, J. H.; MacLachlan, M. J. *Inorg. Chem.* **2006**, *45*, 1442.
(8) (a) Yaghi, O. M.; O'Keeffe, M.; Ockwig, N. W.; Chae, H. K.; Eddaoudi, M.; Kim, J. *Nature* **2003**, *423*, 705. (b) Kitagawa, S.; Kitaura, R.; Noro, S. *Angew. Chem., Int. Ed.* **2004**, *43*, 2334. (c) Férey, G.; Mellot-Draznieks, C.; Serre, C.; Millange, F. *Acc. Chem. Res.* **2005**, *38*, 217. (d) Bradshaw, D.; Claridge, J. B.; Cussen, E. J.; Prior, T. J.; Rosseinsky, M. J. *Acc. Chem. Res.* **2005**, *38*, 273. (e) Mori, W.; Takamizawa, S. In *Organometallic Conjugation*; Nakamura, A., Ueyama, N., Yamaguchi, K., Eds.; Springer: Tokyo, 2002; Chapter 6, p 179.
(9) (a) For current examples of gas adsorption, see: Millange, F.; Serre, C.; Guillon, N.; Férey, G.; Walton, R. I. *Angew. Chem., Int. Ed.* **2008**, *47*, 4100. (b) Tanaka, D.; Nakagawa, K.; Higuchi, M.; Horike, S.; Kubota, Y.; Kobayashi, T. C.; Tanaka, M.; Kitagawa, S. *Angew. Chem., Int. Ed.* **2008**, *47*, 3914. (c) Serre, C.; Millange, F.; Thouvenot, C.; Nogues, M.; Marsolier, G.; Louër, D.; Férey, G. *J. Am. Chem. Soc.* **2002**, *124*, 13519. (d) Chandler, B. D.; Cramb, D. T.; Shimizu, G. K. H. *J. Am. Chem. Soc.* **2006**, *128*, 10403. (e) Braga, D.; Curzi, M.; Johansson, A.; Polito, M.; Rubini, K.; Grepioni, F. *Angew. Chem., Int. Ed.* **2006**, *45*, 142.

Chart 1. One-Dimensional Assembled Structures of **1a**, **1b**, **2a**, and **2b**

$[M^{II}_2(bza)_4(2\text{-}Rpyz)]_n$

R = H, M = Rh^{II} (**1a**)
R = H, M = Cu^{II} (**1b**)
R = Me, M = Rh^{II} (**2a**)
R = Me, M = Cu^{II} (**2b**)

Figure 1. Adsorption isotherms of O₂ (below saturated pressure of liquid O₂) at 77 K for **1a**, **1b**, **2a**, and **2b**: adsorption process (open point), desorption process (solid point).

from those of the bulk O₂ phase.[10] Subsequently, the magnetic properties of adsorbed O₂ in the crystal channels were investigated in combination with the X-ray diffraction structure analysis of the guest aggregate.[11,12] We previously reported the magnetic properties of O₂ molecules in a 1D chain in $[Rh_2(bza)_4(pyz)]_n$ and $[Rh_2(bza)_4(2\text{-}mpyz)]_n$ (bza = benzoate; pyz = pyrazine (**1a**); 2-mpyz = 2-methylpyrazine (**2a**)), which can generate stable O₂-included crystals at low temperature using forcible adsorption conditions and is suitable for single-crystal X-ray analysis.[12–14] In the case of **2a**, the abnormal magnetic behavior was observed for O₂ aggregates under an applied magnetic field.[12] Because the adsorbed O₂ molecules are captured physically by the diamagnetic organic moieties in the narrow channel, the host–guest electrical interactions would be almost negligible, which provide the magnetic information of the included one-dimensional O₂ chain without disturbance. Therefore, these single-crystal adsorbents are a powerful tool for observing both the exact guest aggregate structure and the magnetic behavior of the guest itself.

Herein, we report the O₂ gas adsorbing behavior of the four types of single-crystal adsorbents $[M_2(bza)_4(pyz)]_n$ (**1**) and $[M_2(bza)_4(2\text{-}mpyz)]_n$ (**2**) (M = Rh^{II} (**a**) and Cu^{II} (**b**); **1a**, **1b**, **2a**, **2b**) and the magnetic behaviors of O₂ gases included in the crystal hosts (Chart 1). In order to understand the magnetic behavior in the channels to a greater degree, we determined that the configuration changes of O₂ aggregates by temperature change and their magnetization properties depend on time and temperature.

Results and Discussion

O₂ Gas-Adsorbing Properties of the Crystal Hosts. The adsorption isotherms of O₂ gas were measured on **1a**, **1b**, **2a**,
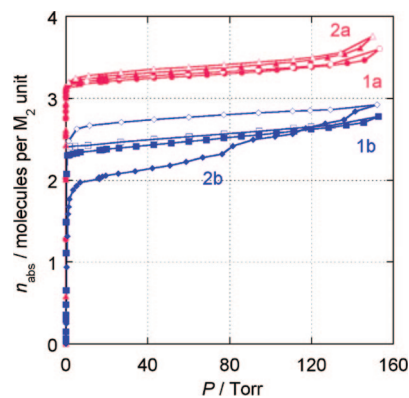
and **2b** at 77 K (Figure 1).[15] The isotherms are reversible and revealed a smooth adsorption at extremely low pressure. The adsorption amounts of O₂ immediately reached three molecules per Rh₂ unit for **1a** and **2a**. In contrast, the Cu compounds of **1b** and **2b** adsorbed around 3 molecules per Cu₂ unit at the saturation pressure, which is slightly below the amounts of O₂ adsorption than that of the Rh compounds in spite of their similarity in O₂-included crystal structures.[14] Compound **2b** cannot easily desorb the adsorbed O₂ and showed a hysteretic adsorption, which indicates a difficulty to transfer a guest gas through the crystal at 77 K. The adsorption amounts of 3 O₂ are in good agreement with those determined by single-crystal X-ray analysis in a pressurized O₂ gas atmosphere (see next section).

O₂-Included Crystal Structures. The crystal structures for O₂-included complexes of **1a** and **2a** were determined by single-crystal X-ray diffraction analysis over a wide temperature range (298,[12] 190,[12] 150, 130, 110, 90,[12,13] 70, 40, 20, and 10 K[12,13]). Precise diffraction studies using fine temperature intervals were performed in order to investigate the correlation between the inclusion structures and the magnetic properties of the included O₂ molecules. The measurements were conducted in a pressurized O₂ gas atmosphere (see the Experimental Section). Crystallographic data are summarized in Tables S1–S2 (Supporting Information), and ORTEP drawings are depicted in Figures S1–S2 (Supporting Information). The O₂-included crystals were determined to be **1a**·3O₂ and **2a**·3O₂ below 190 K for **1a** and **2a**, which corresponds to complete loading of the channel. Figures 2 and 3 are the packing views at 110 K for **1a** and **2a**, and the intersection views for **1a** ($P\bar{1}$ at 150 K) and **2a** ($C2/m$ at 150 K and $P\bar{1}$ at 110 K) are shown as representative examples. In all temperature ranges, the O₂-included crystal of **1a** possesses the space group of $P\bar{1}$, and the structures of the host skeleton of **1a** are essentially the same. This $P\bar{1}$ phase is transformed from $C2/m$ of its nonincluded crystal by the O₂ adsorption.[16] The space group of $P\bar{1}$ at 298 K indicates the inclusion of O₂ molecules in the channel. Thus, the lack of an observable O₂ molecule at 298 K is probably due to the vigorous thermal motions of guest O₂ molecules in the channels.[17] For the included crystal **2a**, the space group changed in the sequence

(10) Mori, W.; Kobayashi, T. C.; Kurobe, J.; Amaya, K.; Narumi, Y.; Kumada, T.; Kindo, K.; Katori, H.; Goto, T.; Miura, N.; Takamizawa, S.; Nakayama, H.; Yamaguchi, K. *Mol. Cryst. Liq. Cryst.* **1997**, *306*, 1.

(11) (a) Kitaura, R.; Kitagawa, S.; Kubota, Y.; Kobayashi, T. C. K; Kindo, K. Y.; Mita, Y. A.; Matsuo, A. M.; Kobayashi, M. H. C.; Chang, H. C. T. C.; Ozawa, T. C. M.; Suzuki, M. M.; Sakata, M. M.; Takata, M. *Science* **2002**, *298*, 2358. (b) Kitaura, R.; Matsuda, R.; Kubota, Y.; Kitagawa, S.; Takata, M.; Kobayashi, T. C.; Suzuki, M. *J. Phys. Chem. B* **2005**, *109*, 23378. (c) Kobayashi, T. C.; Matsuo, A.; Suzuki, M.; Kindo, K.; Kitaura, R.; Matsuda, R.; Kitagawa, S. *Prog. Theor. Phys. Suppl.* **2005**, *159*, 271.

(12) Takamizawa, S.; Nakata, E.; Akatsuka, T. *Angew. Chem., Int. Ed.* **2006**, *45*, 2216.

(13) Takamizawa, S.; Nakata, E.; Saito, T. *Angew. Chem., Int. Ed.* **2004**, *43*, 1368.

(14) Takamizawa, S.; Nakata, E.; Saito, T.; Akatsuka, T.; Kojima, K. *Cryst. Eng. Commun.* **2004**, *6*, 197.

(15) Takamizawa, S.; Nakata, E.; Akatsuka, T.; Miyake, R.; Takeuchi, H.; Maruta, G.; Takeda, S. Submitted for publication.

(16) Takamizawa, S.; Nakata, E.; Yokoyama, H.; Mochizuki, K.; Mori, W. *Angew. Chem., Int. Ed.* **2003**, *42*, 4331.

(17) In **2a**, 2O₂ molecules can be observed even at 298 K due to the close contacts between the guest and the methyl group on the host skeleton.
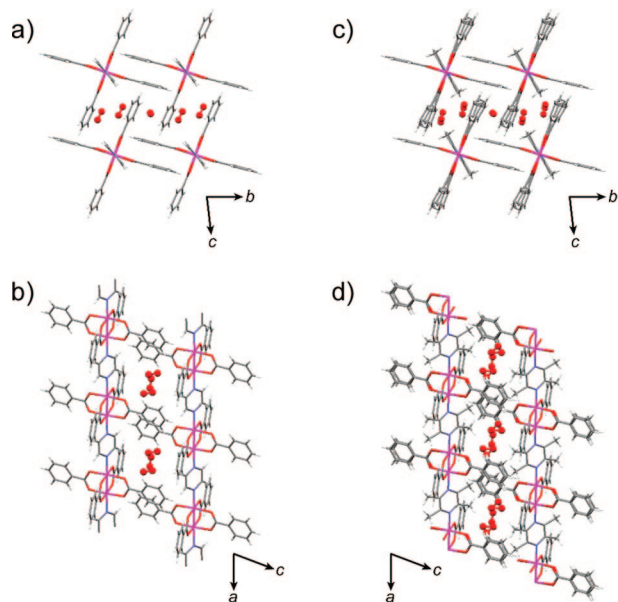
Figure 2. Packing views of O_2-included crystals of **1a** (a, b) and **2a** (c, d) at 110 K (the $P\bar{1}$ phase) showing the projection along the *a* axis (a, c) and *b* axis (b, d). Elements are color-coded: Rh (magenta), C (gray), H (white), N (blue), and O (red). The phenyl groups of **2a** (c) and (d) were disordered.
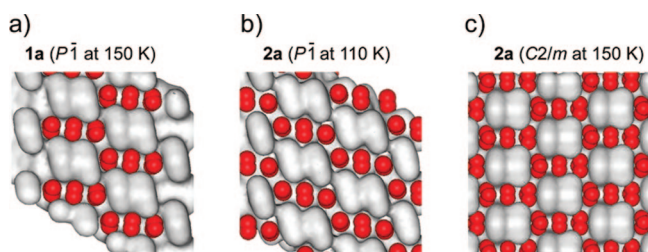

Figure 3. Intersection views for the channel structure: (a) $P\bar{1}$ phase at 150 K for **1a**, (b) $P\bar{1}$ phase at 110 K for **2a**, and (c) $C2/m$ phase at 150 K for **2a**.

of high, $C2/m$ (298−130 K), middle, $P\bar{1}$ (110−40 K), low, $C2/m$ (20−10 K), in the variation of the temperature. The space group of $C2/m$ at 298 K suggests the crystal-phase transition induced by the O_2 adsorption from the $P\bar{1}$ phase of the nonincluded crystal of **2a**. The $P\bar{1}$ phase found in **1a** in all temperature ranges and in **2a** in the middle temperature range of 110−40 K exhibits the similar one-dimensional channel structure. The high- and low-temperature regions ($C2/m$) of **2a** generate isolated cavities (see Figure 3).

Guest−Guest Interactions in the O_2-Included Crystal Adsorbent. In all included crystals, the arrangement of the adsorbed O_2 molecules consists of a repeating trimer, $[O_2(B)\cdots O_2(A)\cdots O_2(B)]$, of which the molecular axes are twisted relative to each other (Figure 4). The interatomic and intermolecular distances in $O_2(A)\cdots O_2(B)$ and $O_2(B)\cdots O_2(B')$ are listed in Table 1 for **1a** and **2a**. For both inclusion crystals, the long molecular axes are twisted from one another between the $O_2(A)\cdots O_2(B)$ molecules. The $O_2(B)\cdots O_2(B')$ molecules aligned parallel to each other with respect to the long axis. On cooling, the molecular axes change slightly depending on the temperature. In **1a**, the adsorbed O_2 molecules were observed without disorder in all temperature ranges except for 10 K. At 10 K, the O_2 molecule in the A site was found in two positions. In contrast, the disordered O_2 molecules in the B site were observed for **2a** in the temperature range of 150−10 K except
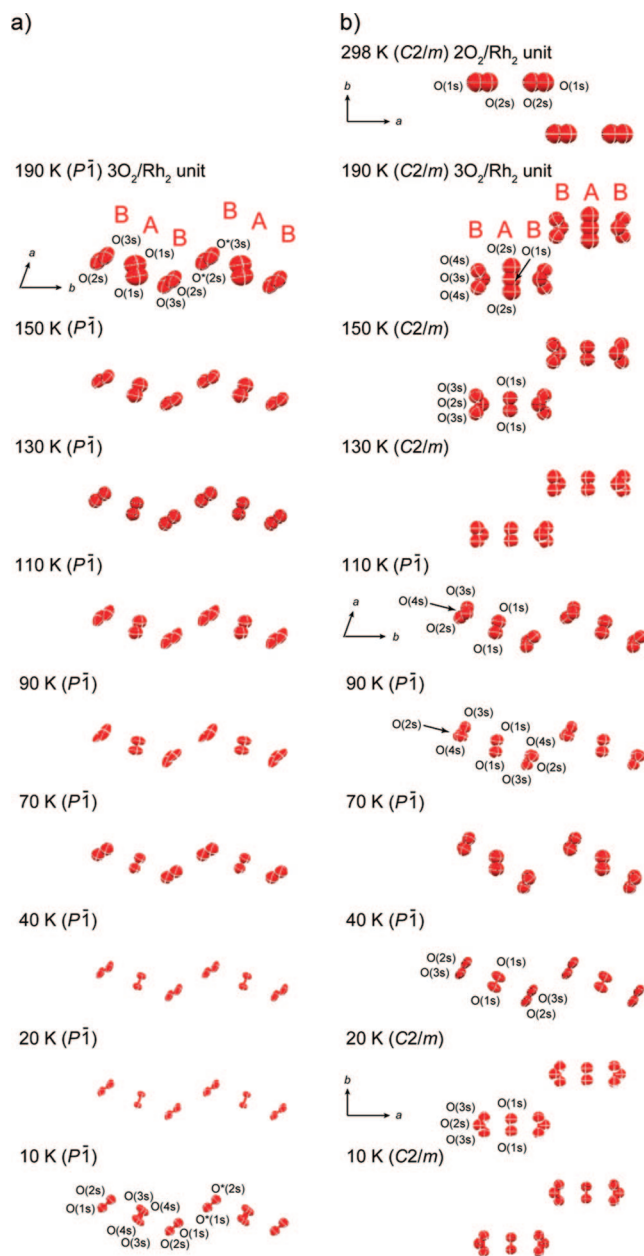

Figure 4. Thermal ellipsoid diagrams for the guest configuration for **1a** (a) and **2a** (b) (50% probability) at various temperatures (190, 150, 130, 110, 90, 70, 40, 20, and 10 K).

for 40 K. The two observed molecular axes for the B site are different from that in **1a**, which are caused by the short contacts with the methyl moiety of the host skeleton. At 190 K, one oxygen atom of the O_2 molecules in both the A and B sites is disordered over two positions. The shortest distances are plotted against the temperature (Figure 5a,b,d,e). The interatomic distances between the neighboring O_2 molecules in **2a** are longer than are those in **1a**. For **1a**, the distances between the centers of the O_2 molecule changed slightly. However, the shortest interatomic contacts between neighboring O_2 molecules sensitive to temperature are in the range of 70−130 K. Below 130 K, the difference in interatomic distance between $O(A)\cdots O(B)$ and $O(B)\cdots O(B')$ was under around 0.2 Å. For **2a**, large changes were observed in both the intermolecular and interatomic distances between 70 and 130 K, which were minimized at 90 and 110 K. These decreases in the intermolecular and inter-atomic distances are expected to increase the one-dimensional

Table 1. Interatomic and Intermolecular Distances (Å) between O$_2$ Molecules Included in the Channels of the Crystals of **1a** and **2a**

1a[a]

	190 K		150 K		130 K	
guest (A)−guest (B)	O(1s)···O(2s)	3.52(10)	O(1s)···O(2s)#1	3.67(2)	O(1s)···O(3s)	3.39(2)
	O(1s)···O(3s)	3.13(10)	O(1s)···O(3s)	3.44(2)	O(1s)···O(3s)#1	3.395(18)
	O(1s)···O(3s)#1	3.62(9)	O(1s)···O(3s)#1	3.247(19)		
guest (B)−guest (B)	O(2s)···O(2s)#2	3.88(7)	O(2s)···O(2s)#2	3.68(4)	O(2s)···O(2s)#2	3.47(4)
intermolecular distance	X(A)···X(B)	3.4668(17)	X(A)···X(B)	3.501(3)	X(A)···X(B)	3.5423(14)
	X(B)···X(B)#2	4.3993(16)	X(B)···X(B)#2	4.247(2)	X(B)···X(B)#2	4.2702(13)

	110 K		90 K		70 K	
guest (A)−guest (B)	O(1s)···O(2s)#1	3.69(4)	O(1s)···O(3s)	3.50(2)	O(1s)···O(2s)	3.68(4)
	O(1s)···O(3s)	3.36(4)	O(1s)···O(3s)#1	3.51(2)	O(1s)···O(3s)	3.28(4)
	O(1s)···O(3s)#1	3.32(3)			O(1s)···O(3s)#1	3.45(5)
guest (B)−guest (B)	O(2s)···O(2s)#5	3.72(6)	O(2s)···O(2s)#2	3.94(3)	O(2s)···O(2s)#2	3.49(7)
intermolecular distance	X(A)···X(B)	3.4806(14)	X(A)···X(B)	3.55	X(A)···X(B)	3.5261(14)
	X(B)···X(B)#5	4.3012(13)	X(B)···X(B)#2	4.24	X(B)···X(B)#2	4.1657(13)

	40 K		20 K		10 K	
guest (A)−guest (B)	O(1s)···O(2s)#1	3.704(10)	O(1s)···O(2s)#1	3.650(11)	O(2s)···O(3s)#3	3.48(4)
	O(1s)···O(3s)#1	3.343(10)	O(1s)···O(3s)#1	3.341(10)	O(2s)···O(3s)#4	3.17(6)
	O(1s)···O(3s)	3.372(12)	O(1s)···O(3s)	3.293(13)	O(2s)···O(4s)#4	3.12(5)
					O(1s)···O(4s)#4	3.44(6)
guest (B)−guest (B)	O(2s)···O(2s)#5	3.548(17)	O(2s)···O(2s)#2	3.530(18)	O(1s)···O(1s)#5	3.37(2)
intermolecular distance	X(A)···X(B)	3.4962(7)	X(A)···X(B)	3.4419(7)	X(A)···X(B)	3.46
	X(B)···X(B)#2	4.2598(6)	X(B)···X(B)#2	4.3846(6)	X(B)···X(B)#5	4.32

2a[b]

	190 K[12]		150 K		130 K	
guest (A)−guest (B)	O(1s)···O(3s)	3.40(6)	O(1s)···O(2s)	3.53(6)	O(1s)···O(2s)	3.72(6)
	O(1s)···O(4s)	3.50(5)	O(1s)···O(3s)	3.59(5)	O(1s)···O(3s)	3.59(7)
	O(2s)···O(3s)	3.58(6)				
	O(2s)···O(4s)	3.43(5)				
guest (B)−guest (B)	O(4s)···O(4s)#6	4.7162(8)	O(3s)···O(3s)#6	4.35(6)	O(3s)···O(3s)#6	4.71(9)
intermolecular distance	X(A)···X(B)	3.38	X(A)···X(B)	3.5388(18)	X(A)···X(B)	3.6232(12)
	X(B)···X(B)#6	5.01	X(B)···X(B)#6	4.7704(18)	X(B)···X(B)#6	4.8412(12)

	110 K		90 K[12]		70 K	
guest (A)−guest (B)	O(1s)···O(2s)#7	3.63(4)	O(1s)···O(2s)	3.59(5)	O(1s)···O(2s)	3.22(5)
	O(1s)···O(3s)	3.42(6)	O(1s)···O(3s)	3.42(3)	O(1s)···O(3s)	3.28(6)
	O(1s)···O(4s)	3.61(6)			O(1s)···O(4s)	3.43(7)
guest (B)−guest (B)	O(2s)···O(2s)#8	4.16(5)	O(2s)···O(4s)#8	4.12(8)	O(4s)···O(4s)#8	4.72(9)
			O(4s)···O(4s)#8	4.01(8)		
intermolecular distance	X(A)···X(B)	3.511(2)	X(A)···X(B)	3.54	X(A)···X(B)	3.4502(9)
	X(A)···X(C)	3.550(2)	X(B)···X(B)#6	4.12	X(A)···X(C)	3.4318(10)
	X(C)···X(C)#8	4.432(2)			X(C)···X(C)#8	5.0464(11)

	40 K		20 K		10 K[12]	
guest(A)−guest(B)	O(1s)···O(2s)	3.50(4)	O(1s)···O(2s)	3.55(4)	O(1s)···O(2s)	3.54(4)
	O(1s)···O(2s)#7	3.56(3)	O(1s)···O(3s)	3.46(4)	O(1s)···O(3s)	3.51(6)
	O(1s)···O(3s)#7	3.49(4)				
guest(B)−guest(B)	O(3s)···O(3s)#8	3.91(5)	O(3s)···O(3s)#6	4.16(5)	O(3s)···O(3s)#6	4.05(6)
intermolecular distance	X(A)···X(A)	3.4919(17)	X(A)···X(B)	3.4745(16)	X(A)···X(B)	3.49
	X(B)···X(B)#8	4.8226(18)	X(B)···X(B)#6	4.8345(19)	X(B)···X(B)#6	4.78

[a] Symmetry codes: #1 (2 − x, −y, −z), #2 (2 − x, 1 − y, −z), #3 (1 − x, −1 + y, z), #4 (1 − x, 1 − y, 1 − z), #5 (2 − x, 1 − y, 1 − z). X(A): center of the O₂ (O(1)−O(1)#1) molecule. X(B): center of the O₂ (O(2)−O(3)) molecule (label of oxygen atoms: see Figure 4). [b] Symmetry codes: #6 (0.5 − x, 0.5 − y, 2 − z), #7 (1 − x, 1 − y, 2 − z), #8 (1 − x, −y, 2 − z). X(A): center of the O₂ (O(1)−O(1)#1 or O(1)−(2) for 190 K) molecule. X(B): center of the O₂ (O(2)−O(3) or O(3)−O(4) for 190 K) molecule. X(C): center of O₂ (O(2)−O(4) (for 110, 70 K)) molecule (label of oxygen atoms: see Figure 4).
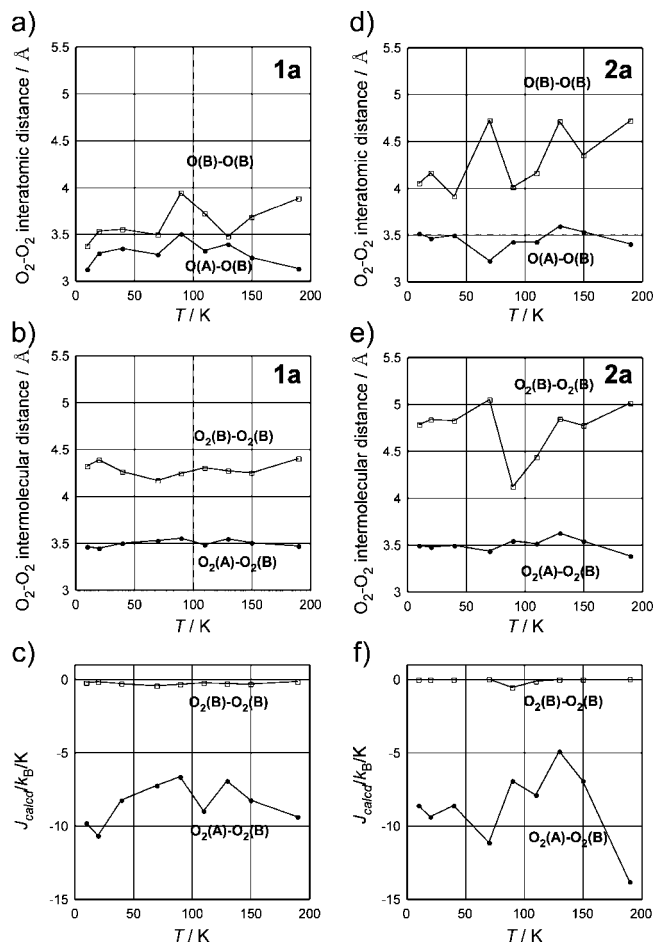
Figure 5. Shortest intermolecular and interatomic distances between neighboring O_2 molecules plotted against temperature for **1a** (a, b) and **2a** (d, e). The calculated intermolecular interactions are based on the intermolecular distance R between the centers of the O_2 molecules for **1a** (c) and for **2a** (f).[12]

character in the molecular chain. Between 70 and 130 K, the guest configurations for **1a** and **2a** are similar in distance between neighboring molecules. Despite the lack of phase transition of the host crystal for **1a** in contrast to the phase transition ($C2/m$ (298−130 K), $P\bar{1}$ (110−40 K) and $C2/m$ (20−10 K)) for **2a**, the structural changes in the guest configuration occurred at the same temperatures between 70 and 130 K for both crystals in terms of distance. Therefore, the configuration is mostly related to the properties of the included O_2 molecule itself.

Host−Guest Interactions in the O_2-Included Crystal Adsorbent. Host−guest contacts are depicted in Figure 6 for the $P\bar{1}$ phase at 110 K of **1a**, for the $P\bar{1}$ phase at 110 K of **2a**, and for the $C2/m$ phase at 150 K of **2a**, as a representative example. The interatomic distances between the host and guest are summarized in Tables 2 and 3 for Figure 6. The other contacts at all temperatures are listed in Tables S3−S4 (Supporting Information). No remarkable changes were observed in the intermolecular contacts between host and guest throughout the entire temperature range. The host−guest contacts observed in **1a** are almost identical for the crystal structures determined at all temperatures in terms of the contacting atoms and the bond distances. In the A site, the O_2 molecule is surrounded by the C(4)−C(5) and C(5)−C(6) atoms from two benzoate moieties ($O_{oxygen}\cdots C = 3.20−3.41$ Å). The O_2 molecules in the B site contact the C(1), C(2), C(8), C(9), and O(1) atoms
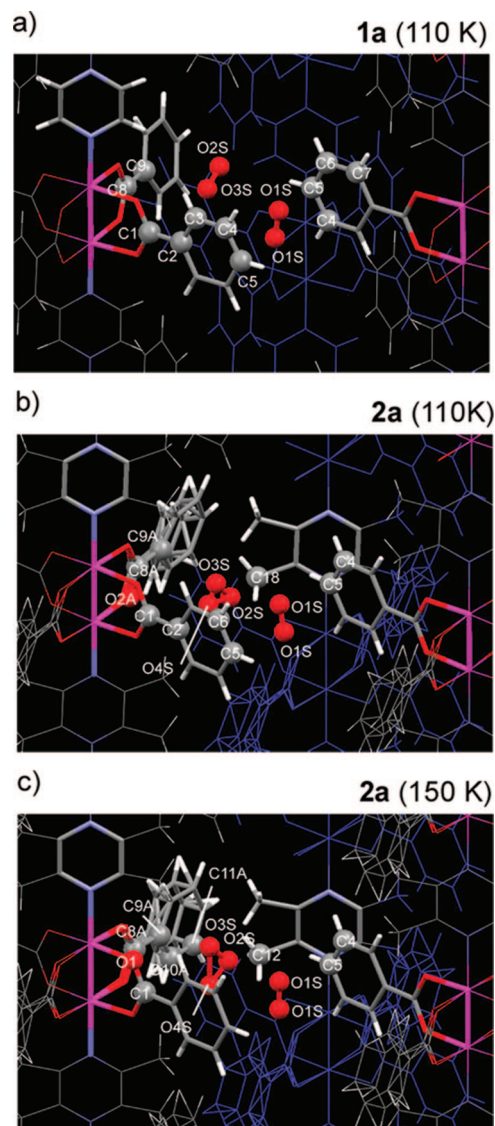
Figure 6. Short interatomic contacts between host and guest: (a) $P\bar{1}$ phase at 110 K for **1a**; (b) $P\bar{1}$ phase at 110 K for **2a**; (c) $C2/m$ phase at 150 K for **2a**.

on the benzoate molecule ($O_{oxygen}\cdots C = 3.22−3.49$ Å, $O_{oxygen}\cdots O = 3.34−3.46$ Å,). In the O_2-included crystal **2a**, the short contacts were found between the O_2 molecule and the methyl group on the host skeleton. The distances range from 2.89 to 3.49 Å between O_2 and C(12) for the $C2/m$ phase and C(18) for the $P\bar{1}$ phase. These contacts will effectively stabilize the included O_2 molecule, which enables crystallographic observation of the guests even at 298 K. For the $C2/m$ phase in **2a**, the O_2 molecules located near the C(4), C(5), C(8), and C(9) atoms ($O_{oxygen}\cdots C = 2.95−3.44$ Å). The contact atoms between the host wall and the O_2 molecules were changed slightly in the $P\bar{1}$ phase of **2a**. Short distances were found between the O_2 molecule and C(4)−C(5), C(5)−C(6), C(13) (for the A site), C(1), C(2), C(8), C(9), and O(1) (for the B site) atoms ($O_{oxygen}\cdots C = 3.26−3.46$ Å for the A site, $O_{oxygen}\cdots C = 3.08−3.47$ Å) for the B site below 190 K. Although large changes in configuration of around 0.5 Å were observed in the guest−guest contacts in the temperature ranges of 130−110 K and 70−40 K, corresponding changes were not found between host and guest, where the differences in interatomic distances were within around 0.3 Å.

Table 2. Interatomic Distances (Å) between Host Skeletons and Guest Molecules for **1a** at 110 K ($P\bar{1}$)[a]

110 K ($P\bar{1}$)			
guest(A)−host		guest(B)−host	
O(1s)···C(5)	3.273(16)	O(2s)···C(9)#4	3.40(2)
O(1s)···C(6)	3.243(14)	O(2s)···H(5)#2	2.90(2)
O(1s)···C(4)#2	3.271(13)	O(2s)···H(14)#3	2.95(3)
O(1s)···C(5)#2	3.320(18)		
O(1s)···H(11)#6	3.175(10)	O(3s)···C(1)	3.29(2)
O(1s)···H(13)#1	3.16(2)	O(3s)···C(2)	3.49(2)
		O(3s)···C(8)#4	3.32(2)
		O(3s)···O(1)	3.40(2)
		O(3s)···O(4)	3.45(2)
		O(3s)···H(10)#5	3.25(4)
		O(3s)···H(11)#5	3.12(4)
		O(3s)···H(14)#3	3.39(3)

[a] Symmetry codes: #1 ($1 - x, -y, 1 - z$), #2 ($2 - x, -y, -z$), #3 ($1 + x, y, -1 + z$), #4 ($1 - x, 1 - y, 1 - z$), #5 ($2 - x, 1 - y, -z$), #6 ($x, y, -1 + z$).

Magnetic Properties of Adsorbed O₂ Molecules. The dc magnetic susceptibilities of O₂ molecules included in **1a**, **1b**, **2a**, and **2b** were measured in a temperature range of 2.0 to 250 K sealed with a high pressure of O₂ (*ca.* 2 MPa at room temperature). The $M(O_2)T$ versus T plots under applied magnetic fields from 1 to 7 T are shown in Figure 7 ($M(O_2)- T$ plots are depicted in Figure S3, Supporting Information). In spite of the differences in the host skeletons of all crystal hosts, the adsorbed O₂ molecules exhibit similar magnetic behavior. The low $M(O_2)T$ value of **2b** may indicate the lower adsorption amounts of O₂ molecules, which is consistent with the results in adsorption measurement. On cooling, the product $M(O_2)T$ under an applied magnetic field of 1 T gradually increases to reach a plateau with a maximum value of around 0.86, 0.86, 0.84, and 0.55 emu·mol⁻¹·Oe·K between 50 and 140 K and then decrease to 0.19, 0.18, 0.09, and 0.08 emu·mol⁻¹·Oe·K at 2 K for **1a**, **1b**, **2a**,[12] and **2b**, respectively (Figure 7). The magnetic behaviors can be divided into three temperature regions from 2 to around 55 K (low), from around 55 to 140 K (middle), and from 140 to 250 K (high) (Figures S4−6, Supporting Information). The decrease of $M(O_2)T$ above 140 K is probably related to the desorption of O₂ molecules. In the middle temperature region, the susceptibility obeys the Curie−Weiss law with C = 0.93, 0.96, 1.09, and 0.75 emu·K·mol⁻¹ and $\theta = -7.60$, -13.0, -8.64, and -45.9 K for **1a** (56−104 K), **1b** (56−106 K), **2a** (54−104 K),[12] and **2b** (50−104 K), respectively. The obtained C values for **1a**, **1b**, and **2a** are in good agreement with the spin-only value of 1.00 emu·K·mol⁻¹ for an O₂ molecule ($g = 2$). The negative Weiss constants indicate the weak antiferromagnetic interaction between neighboring O₂ molecules. Below these temperatures (low-temperature region), the Weiss constants were changed to $\theta = -20.0$, -33.4, -16.9, and -10.9 K for **1a**, **1b**, **2a**,[12] and **2b**, respectively, which suggests an increase of intermolecular antiferromagnetic interactions expect for **2b**. The exchange coupling constants between the O₂ molecules based on mean field approximation,[18] J/k_B, are -4.28, -7.31, -4.86, and -25.8 K in the middle-temperature region, and -11.3, -18.8, -9.48 and -6.13 K in the low-temperature region for **1a**, **1b**, **2a**,[12] and **2b**, respectively. The antiferromagnetic interactions calculated from the inter-molecular distance are plotted in Figure 5 (c) for **1a** and (f) for

(18) On the basis of the following equation, $J/k_B = 3\theta/(2zS(S + 1))$, with $z = 4/3$, where z is the number of nearest neighbors and J is defined by $H = -2J\mathbf{S}_i\mathbf{S}_j$.

Table 3. Interatomic Distances (Å) between Host Skeletons and Guest Molecules for **2a** at 150 K ($C2/m$) and 110 K ($P\bar{1}$)[a]

150 K ($C2/m$)			
guest(A)−host		guest(B)−host	
O(1s)···C(4)	3.326(13)	O(2s)···C(12)#1	3.22(7)
O(1s)···C(5)	3.32(2)	O(2s)···H(8A)#1	3.005(15)
O(1s)···C(9B)#1	3.40(2)	O(2s)···H(12A)#1	2.94(4)
O(1s)···H(8B)#1	3.213(3)		
		O(3s)···C(1)	3.36(3)
		O(3s)···C(6A)	3.24(5)
		O(3s)···C(7A)	3.29(7)
		O(3s)···C(8A)	3.46(7)
		O(3s)···C(8A)#1	3.18(4)
		O(3s)···C(9A)#1	3.15(5)
		O(3s)···C(12)	3.45(5)
		O(3s)···O(1)	3.39(2)
		O(3s)···O(2A)	3.31(5)
		O(3s)···H(8B)#1	3.05(3)
		O(3s)···H(12A)	2.93(3)
		O(3s)···H(12C)	3.10(3)

110 K ($P\bar{1}$)			
guest(A)−host		guest(B)−host	
O(1s)···C(5)#2	3.31(3)	O(2s)···C(9A)#2	3.43(3)
O(1s)···C(6)#2	3.31(2)	O(2s)···C(18)#5	2.94(4)
O(1s)···C(4)#3	3.32(3)	O(2s)···H(5)#3	3.16(3)
O(1s)···C(5)#3	3.33(2)	O(2s)···H(10A)#5	2.77(2)
O(1s)···C(11B)	3.46(5)	O(2s)···H(17B)#6	2.95(2)
O(1s)···C(13B)#4	3.35(3)	O(2s)···H(18B)#5	2.75(2)
O(1s)···H(11B)	2.73(3)		
O(1s)···H(13B)#4	2.797(13)		

guest(B)−host		guest(B)−host	
O(3s)···C(1)#2	3.41(4)	O(4s)···C(1)#2	3.08(3)
O(3s)···C(8A)#2	3.24(6)	O(4s)···C(2)#2	3.30(3)
O(3s)···C(9A)#2	3.31(6)	O(4s)···C(8A)#2	3.21(4)
O(3s)···C(13A)#4	3.25(7)	O(4s)···C(9A)#2	3.46(4)
O(3s)···C(14A)#4	3.30(7)	O(4s)···C(18)#2	3.45(8)
O(3s)···H(13A)#4	2.60(6)	O(4s)···O(1)#2	3.16(3)
O(3s)···H(14A)#4	2.70(6)	O(4s)···O(2A)#2	3.23(5)
O(3s)···H(14B)#4	3.10(7)	O(4s)···H(10A)#5	3.18(4)
		O(4s)···H(13A)#4	3.17(6)
		O(4s)···H(18A)#2	3.08(6)
		O(4s)···H(18C)#2	2.94(5)

[a] Symmetry codes: #1 ($0.5 - x, 0.5 - y, 2 - z$), #2 ($x, -1 + y, z$), #3 ($1 - x, 2 - y, 2 - z$), #4 ($2 - x, 1 - y, 2 - z$), #5 ($1 - x, 1 - y, 2 - z$), #6 ($x, -1 + y, 1 + z$).

2a, which calculation is based on the empirical rule between J/k_B and the intermolecular distance in bulk O₂ solid.[19] As shown in Figure 5, intratrimer distances (O₂(A)···O₂(B)) contributed to the antiferromagnetic interaction between the O₂ molecules while the intertrimer distances (O₂(B)···O₂(B′)) changed by the temperature contributed little. The change of antiferromagnetic interaction is inconsistent with that of the Curie−Weiss plots. This indicates that the observed magnetic interaction is correlated to not only the configuration of O₂ aggregates determined by X-ray analysis under no magnetic field but also by the molecular motion induced by both temperature and an external magnetic field.

Upon increasing the magnetic field, a discontinuity in magnetic susceptibility was observed with the boundary

(19) The correlation for solid oxygen between the antiferromagnetic interaction (J) and the intermolecular distance (R) between O₂ molecules: $J = J_0 \exp\{-\alpha(R- R_0)\}$, where $J_0/k_B = -30$ K, $\alpha = 4.3$ Å⁻¹, $R_0 = 3.2$ Å, in ref 1.
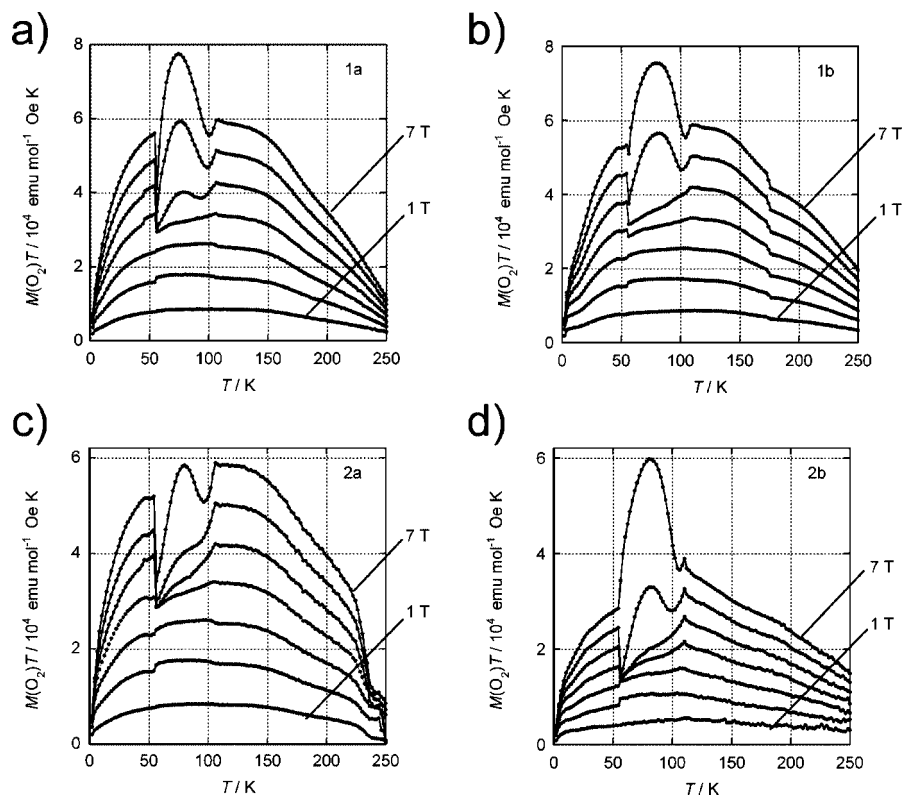
Figure 7. $M(O_2)T$ versus T plots of **1a** (a), **1b** (b), **2a** (c),[12] and **2b** (d) in an applied magnetic field ranging from 1 to 7 T.
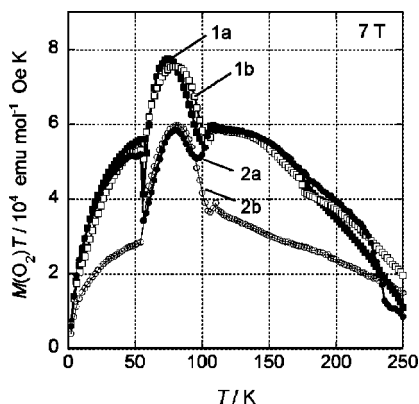

Figure 8. $M(O_2)T-T$ plots of **1a** (solid square), **1b** (open square), **2a** (solid circle),[12] and **2b** (open circle) in an applied magnetic field of 7 T.

temperatures of 56 and 107 K for **1a**, of 56 and 108 K for **1b**, of 56 and 106 K for **2a**,[12] and of 54 and 110 K for **2b**. This indicates the growth of different magnetic states in this temperature region. The boundary temperatures were very similar in this series, but the magnetic behaviors were significantly different from each other in these temperature regions. As shown in Figure 8, at an applied magnetic field of 7 T, $M(O_2)T$ decreases once and abruptly increases to reach a maximum value of 7.75, 7.46, 5.66, and 5.75 emu·mol^{-1}·Oe·K at 74, 80, 80, and 80 K. Then it decreases to 4.13, 5.09, 3.42, and 2.82 emu·mol^{-1}·Oe·K at 56, 56, 56, and 52 K, for **1a**, **1b**, **2a**,[12] and **2b**, respectively, and finally reaches the normal values expected from the magnetic behavior at 1 T. The maximum $M(O_2)T$ value over 7.00 emu·mol^{-1}·Oe·K for **1a** and **1b** can be indicative of the weak ferromagnetic coupling between O_2 molecules in this temperature region. Based on the O_2-inclusion structure, the O_2 molecules are in near-perpendicular geometries between

the A and B sites (the crossed X structure). Theoretical study indicates that this configuration can exhibit ferromagnetic interaction,[20−22] while the weak antiferromagnetic interaction was estimated from the Curie–Weiss fitting of the $\chi^{-1}-T$ plot under 1 T in the middle temperature range. The corrugated change of $M(O_2)T$ will be correlated to the magnetic response from the configuration change of the included O_2 molecules. Furthermore, in this temperature range, because the motion of the O_2 molecules in the channel is activated by temperature, the configuration change combined with the molecular motion can vary the magnetic interaction. This depended on the applied field, and remarkably appeared above 4 T of an applied magnetic field. Three different magnetic states can be observed even at 1 T in the same temperature region, as shown in the $M(O_2)^{-1}-T$ plot. It is worth noting that the observed boundary temperature was very similar along the series and was also independent of the applied magnetic field and the crystal phase transition ($C2/m - P\bar{1} - C2/m$) observed in **2a**. The boundary temperature was similar to that of the phase-transition of bulk oxygen (melting point (T_{mp}): 54.8 K, boiling point (T_{bp}): 90.2 K). Thus, these three states of O_2 aggregates can be understood in terms of the gas, liquid, and solid states of bulk oxygen. The state of O_2 aggregates would be gas adsorption equilibrium state at a high temperature region, a saturated condition with high flexibility at a middle temperature region and 3D ordered cocrystal state at a low temperature region. Thus, there would be a mechanism to help the smooth structural phase transition of O_2 aggregates in the channels physically separated by the host channel walls. The flexibility of the channels should

(20) Bussery, B.; Wormer, P. E. S. *J. Chem. Phys.* **1993**, *99*, 1230.
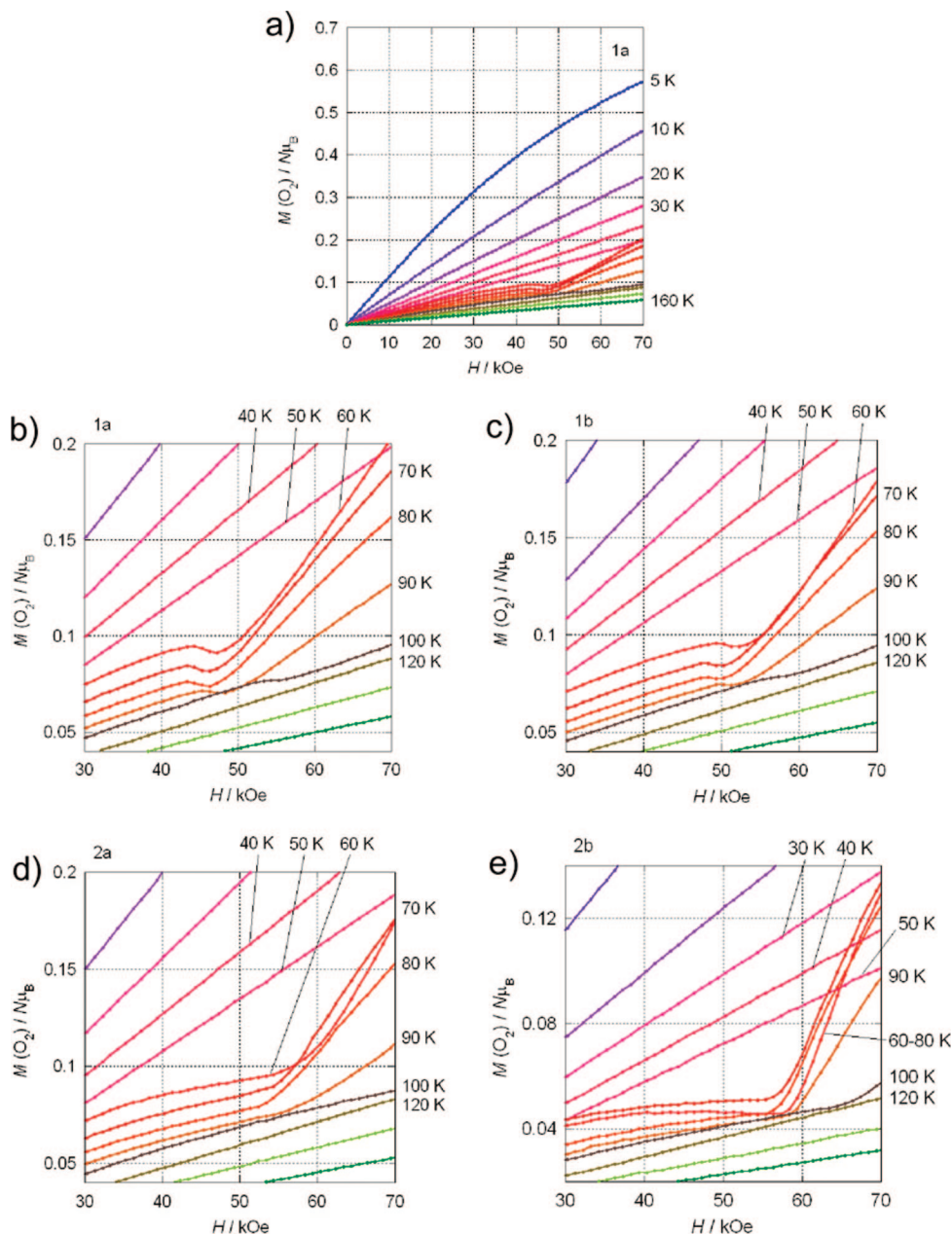(21) Okumura, M.; Yamanaka, S.; Mori, W.; Yamaguchi, K. *THEOCHEM* **1994**, *310*, 177.

Figure 9. Field dependence of magnetization for **1a** in the temperature range of 5−160 K (a); magnified plots of the bending magnetization curves of **1a** (b), **1b** (c), **2a** (d),[12] and **2b** (e).

realize the cooperative support for the local structural change of the aggregates and its spread over the whole crystal.

On the $M(O_2)$ versus H curves, magnetic anomalies were observed above about 4 T between 60 and 100 K for all inclusions (Figures 9 and S7, Supporting Information). This boundary temperature is consistent with that showing the abnormal $M(O_2)T-T$ curve in the observed range of the applied magnetic field. As the magnetic field increased, the increase in magnetization slowed. Then the minimum in the curve for **1a** (at around 4.5 T) and **1b** (at around 5 T), and the bending curve for **2a**[12] and **2b** at around 5.5 T were observed. Beyond this critical magnetic field, the magnetization increased rapidly. The inflection point for **2** was observed at a higher magnetic field than that for **1** by about 1 T. This magnetic change is very slow in the middle temperature range, and shows a hysteresis loop (at 60 K, Figure 10).

At 60 K, a hysteresis loop appears at a critical magnetic field of 4.4 and 5.6 T for **1a** and **2a**,[12] respectively. For **1a**, the hysteresis loop is inverted between 4.4 and 4.6 T. This is probably due to the configuration of O_2 that enhances the intermolecular antiferromagnetic interaction induced by this applied magnetic field. After passing over the critical magnetic field, the magnetization curve increased perpendicularly and showed no inverted hysteresis. This indicates the relaxation of antiferromagnetic interaction between included the O_2 molecules over the critical magnetic field. The magnetization curves for **2a** also figures essentially the similar magnetization curves but the shape and bending field are significantly different. These hysteresis behaviors suggest the influence of a structural difference in the channel and the different pathways in the configuration change of guests in the channel between **1a** and **2a**.
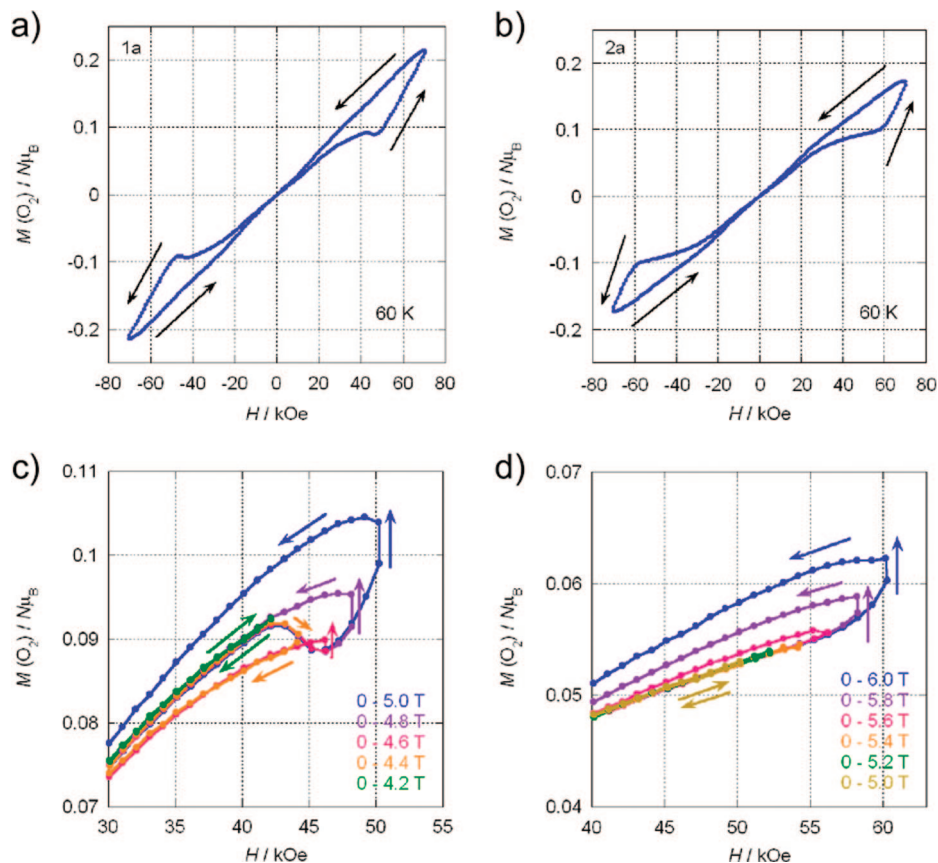
Figure 10. $M(O_2)$-H plots for **1a** (a) and **2a** (b)[12] at 60 K. Magnetization under different ranges of the applied magnetic field: (c) from 0 to 4.2, 4.4, 4.6, 4.8, and 5.0 T for **1a** and (d) from 0 to 5.0, 5.2, 5.4, 5.6, 5.8, and 6.0 T for **2a**.
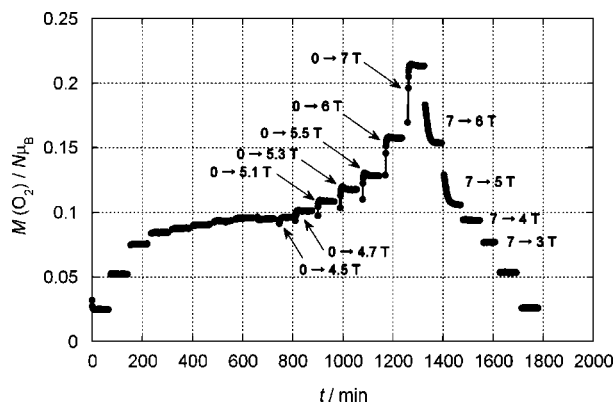

Figure 11. Time course of magnetization $M(O_2)/N\mu_B$ for **1a** at 60 K. The applied magnetic field increased from 0 T to 1.0, 2.0, 3.5, 3.7, 3.9, 4.1, 4.3, 4.5, 4.7, 4.9, 5.1, 5.3, 5.5, 6.0, and 7.0 T. In the decreasing magnetization process, the applied magnetic field ranged from 7.0 T to 6.0, 5.0, 4.0, 3.0, 2.0, and 1.0 T.

Time Course of Magnetization. The hysteresis curves indicate the magnetization depending on the magnitude of the field and time. In order to study the change of magnetization, the time course of the magnetic moment for **1a** was measured under various applied magnetic fields at 60 K (Figure 11).

As the applied magnetic field was increased from 0 T, magnetization depending on time was observed in the applied magnetic field ranges above 4.5 T. Once the magnetic field was applied, the magnetization immediately increased and reached equilibrium when passing the peak. In consideration of the intermediate magnetic state I, the A→I→B sequence

Table 4. Half-Lives for the Generation of First Magnetization A(A→I) and Second Magnetization B and Their Equilibrium Values

applied magnetic field (T)	half-life (min)		saturation magnetization ($N\mu_B$)	
	A→I	I→B	I	B
0−7	1.53	25.5	0.215	0.213
0−6	1.60	15.2	0.159	0.157
0−5.5	1.23	8.36	0.133	0.128
0−5.3	1.33	9.58	0.122	0.117
0−5.1	1.33	8.60	0.111	0.108
0−4.9	1.31	8.38	0.102	0.101
0−4.7	1.47	22.7	0.094	0.095
0−4.5	1.28	15.8	0.094	0.095

applied magnetic field (T)	B→A	B
7−6	7.87	0.152
7−5	8.27	0.105

on the first-order rate constant was approximately applied for the magnetization process. The time dependence of magnetization $M^H(t)$ at magnetic field H is presented as the following equation

$$A \xrightarrow{k_1} I \xrightarrow{k_2} B$$

$$M^H(t) = M^H_A[A] + M^H_I[I] + M^H_B[B]$$

$$[A] + [I] + [B] = 1$$

$$M^H(t) = M^H_A e^{-k_1 t} + M^H_I \{k_1/(k_1 - k_2)\}\{e^{-k_2 t} - e^{-k_1 t}\} +$$

$$M^H_B[1 + \{k_2/(k_1 - k_2)\}e^{-k_1 t} - \{k_1/(k_1 - k_2)\}e^{-k_2 t}]$$

where M^H_A is the magnetization of the beginning state A, M^H_I is the magnetization of the intermediate state I, and M^H_B
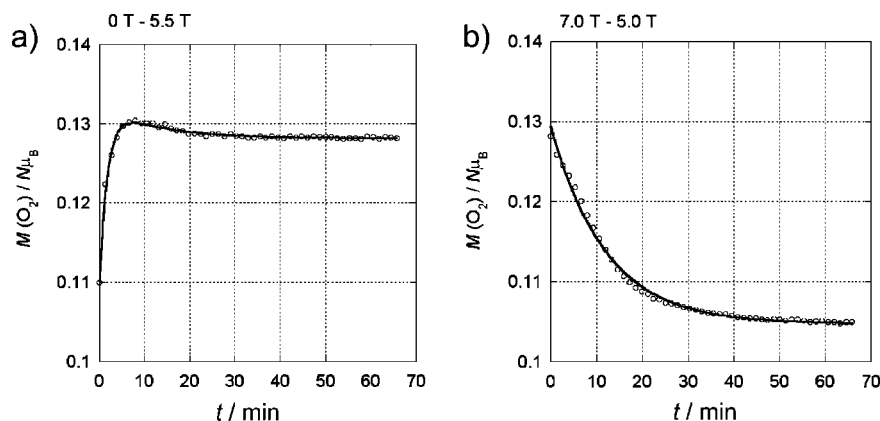
Figure 12. Increasing and decreasing magnetization processes at the applied field from 0 to 5.5 T (a) and from 7.0 to 5.0 T (b), respectively, as representative examples. The solid lines are the fittings based on approximation to the A→I→B process (a) and the A→B process (b) discussed in the text.

is the magnetization of the final state B. k_1 and k_2 are the constants of the translation rate for components A→I and I→B, respectively.[23] These constants were estimated by a curve fitting method (Table 4). We estimate the translation rate as the half-life t of the magnetization from the constants k ($t = (\ln 2)/k$) since k_1 and k_2 are not the rate constant, although they are proportional to the rate constant. The fitting curves are depicted in Figure 12 (a) for 0−5.5 T and Figure S8 (Supporting Information) for the other curves, which fitted the observed curves well. This treatment reproduces the time course of magnetization, which indicates the three magnetic states (A, I, and B) possessing the distinctive structures, respectively.

Above 4.9 T, component I shows a slightly higher value of the equilibrium magnetization than does the second component B. The magnetic state of I is achieved during the first stage, having a half-life of around 1.5 min in all ranges of the applied magnetic field. The magnetization finally reached equilibrium state B with a longer half-life of I(I→B) than that estimated for A(A→I). Thus, the intermediate state I was initially populated before translation to the B state. For component B, similar values were obtained in the magnetic field range of 5.1−5.5 T. The half-lives of B at 4.5, 4.7, 6.0, and 7.0 T are longer than those observed for 4.9−5.5 T, which are expected from the generation of different magnetic states depending on the applied magnetic field. The changes of half-lives between 4.5 and 4.9 T are probably related to the existence of the inversion point of the hysteresis loop between 4.4 and 4.6 T.

As the magnetization process decreased from 7 T, the slow time course of the magnetic moment was observed under the applied magnetic field ranges of 7−6 and 7−5 T. Although this process is the inverse course of the increasing magnetization process (B→I→A), the intermediate magnetic phase I apparently cannot be observed. This indicates the fast conversion from I to A compared to that from B to I. Therefore, we can approximate that the magnetic state changes from component B to A. Thus, we apply the following equations for the time course of magnetization

$$B \xrightarrow{k_1} A$$
$$M^H(t) = M^H_B[B] + M^H_A[A]$$
$$[B] + [A] = 1$$
$$M^H(t) = M^H_B e^{-k_1 t} + M^H_A(1 - e^{-k_1 t})$$

where M^H_A is the magnetization of the A state, M^H_B is the magnetization of the B state, and k_1 is the constant of the

translation rate for the component [B].[22] The component [A] is defined as the initial value of magnetization, $M/N\mu_B = 0$. The results of fitting are depicted in Figures 12b and S8 (Supporting Information) and are also summarized in Table 4. To reach the equilibrium state of [B], the half-life can be estimated to be about 8 min for both the magnetic field ranges of 7.0−6.0 and 7.0−5.0 T. Interestingly, when the data are collected 50 min after the application of the magnetization that is sufficient to trace the equilibrium magnetic states while the magnetic fields are varied, the hysteresis loop actually disappears (see Figure S9, Supporting Information). Thus, the hysteresis curve should be observed in the $M(O_2)-H$ curve because of the relaxation process and suggests that the guest configuration changed from the intermediated state I to the final state B. Considering that the phase transitions of bulk oxygen occur at 54.8 K (T_{mp}) and 90.2 K (T_{bp}), the magnetic phases of the middle temperature ranges for included O₂ molecules correspond to the mesophase between the solid and fluid state. Thus, the adsorbed O₂ molecules will form soft aggregates in the channel. Although the changes of magnetization indicated changes in the magnetic interaction of the O₂ aggregates that were induced by magnetic anisotropy, the energy difference in the change of the configuration of the included O₂ aggregates is too low to be observed under the condition in which the applied magnetic field is low and the temperature of the measurement is high compared with the magnetic anisotropic energy of the O₂ molecules ($D = 5.8$ K for the gas phase).[24] These results suggest that the flexible host stabilizes the configuration of the O₂ aggregates, which enable observation of the states of slightly different energy levels.

Conclusion

In this series, we revealed the configurations and magnetic behaviors of the adsorbed O₂ molecules. We can control the configuration of pseudo-1D O₂ aggregates by modifying the crystal host, which induces differences in the channel structure. These structural differences are related to differences in magnetic behaviors, the $M(O_2)T-T$ curve slope, the critical magnetic fields on the $M(O_2)-H$ curve, and hysteresis behavior. On the other hand, interestingly, similar abnormal magnetic behaviors were observed from the included O₂ molecules in all adsorbents (**1a**, **2a**, **1b**, **2b**), which have different metals and substituents, implying involvement in the different channel structures.

Depending on the applied magnetic field above 4.5 T in the temperature range of 55−105 K, these magnetic susceptibilities were clearly changed. Considering that the boundary temperatures were similar to those of the phase-transition

temperatures of bulk O_2, the three states of O_2 aggregates observed under applied magnetic fields can be categorized into three phases (gas equilibrium state for high temperature (>105 K), soft aggregate state for middle temperature ($55-105$ K), 3D ordered cocrystal state for low temperature (<55 K)). Since guest aggregation with fluidity is expected to be generated in this temperature range, these results strongly supported our hypothesis that these abnormal magnetic behaviors were caused by changes in the configuration of the adsorbed O_2 molecules induced by the external magnetic field, as was described in the result for **2a**.[12] This was also suggested by detailed structural analyses for **1a** and **2a** at fine temperature intervals and the facts that the changes in the host−guest and guest−guest contacts and the differences in the inclusion structure between **1a** and **2a** were slight. The hysteresis loop on the $M-H$ curve indicates a time-dependent magnetization process for these magnetic changes. These facts suggested the existence of the short-life intermediate state of the O_2 aggregates in the channels. Although the observed magnetic property can be induced by a change in the guest configuration due to the magnetic anisotropy of paramagnetic O_2, the observed phenomena cannot be measured at the relatively high temperature and low applied magnetic field for the small energy difference expected for the magnetic anisotropy of O_2. Considering that such a low energy phenomenon was observed, these series of flexible single-crystal hosts distinguish and stabilize the alternative guest configuration by the slight change of condition. The guest structural change and the host structural change can be coupled in small-energy scale phenomena. Therefore, by using the flexible host solids, there is great possibility to observe diverse specific quantum effects in the light aggregates by signal enhancement to perceptible bulk level. To truly understand these phenomena, single-crystal X-ray analysis under a magnetic field would be needed to clear the exact aggregate structures in the magnetic field, and is currently an attractive subject for study.

Experimental Section

Single-Crystal X-ray Diffraction Experiment. Single crystals of **1a** and **2a** were prepared by the reported method.[12,25] Measurements were conducted on a Bruker SMART APEX CCD area (graphite-monochromated Mo Kα radiation, $\lambda = 0.71073$ Å) with a nitrogen flow temperature controller. Using a liquid nitrogen bath, the single crystal was sealed inside a thick-walled glass capillary with condensed O_2 gas. The inner pressure of the O_2 gas was estimated from the ratio of the volume of liquid O_2 and inner space, giving ca. 9 MPa for **1a** and ca. 1 MPa for **2a** at room temperature. Data collections were performed at 20, 40, 70, 110, 130, and 150 K for **1a** and **2a** and at 190 K for **2a**. Empirical absorption corrections were applied using the SADABS program. The structures were solved by direct methods (SHELXS 97) and refined by full-matrix least-squares calculations on F^2 (SHELXL-97) using the SHELX-TL program package. The DFIX command was used to restrain the O−O distance of an O_2 molecule (1.15 Å). Non-hydrogen atoms were refined anisotropically; hydrogen atoms were fixed at calculated positions and refined using a riding model. The crystallographic data of the structure determination collected under different conditions are summarized in Table 1. CCDC-641540−641553 (**1a**: 190 K (641540), 150 K (641541), 130 K (641542), 110 K (641543), 70 K (641544), 40 K (641545), 20 K (641546), **2a**: 150 K (641547), 130 K (641548), 110 K (641549), 70 K (641550), 40 K (641551), 20 K (641552), 10 K (641553)) contains the supplementary crystallographic data for this paper.

Physical Measurements. The adsorbents of **1b** and **2b** were synthesized as described elsewhere.[15,25−28] O_2 (99.99% purity) was used during the physical measurements. Adsorption isotherm measurements of O_2 for **1a**, **1b**, **2a**, and **2b** were performed by a volumetric method at 77 K in a pressure range from 0.002 to 153 Torr on a Quantachrome Autosorb-1 MP. Measurement of magnetic susceptibility was performed on a Quantum Design SQUID magnetometer MPMS-XL. The dc measurements were conducted from 2 to 250 K under an applied magnetic field from 1 to 7 T. Crystals of **1a**, **1b**, **2a**, and **2b** were packed in a glass tube with pressurized O_2 gas at 298 K (ca. 2.0 MPa for all samples). The crystalline sample in the glass tube can separate from the condensed excess O_2. Measurement of the pure O_2 was performed by using the sample tube containing O_2 with an inner pressure of ca. 2.0 MPa at 298 K. Susceptibility was corrected based on the trace background values of the cell and the nonincluded crystals. The molar magnetization and susceptibility of the adsorbed O_2 were calculated from $3O_2/M_2$ unit determined by single-crystal X-ray analysis.

Supporting Information Available: Additional X-ray structure and additional magnetic spectral data of O_2-included crystal hosts. This material is available free of charge via the Internet at http://pubs.acs.org.

JA806257M

(22) Kawakami, T.; Takamizawa, S.; Takenaka, M.; Nishimura, Y.; Kitagawa, Y.; Okumura, M.; Mori, W.; Yamaguchi, K. *Polyhedron* **2007**, *26*, 2367.
(23) The variable time *t* includes the time lag for the measurement (ca. 3.5 min).
(24) Kimura, S.; Kindo, K.; Narumi, Y.; Hagiwara, M.; Kikuchi, H.; Ajiro, Y. *J. Phys. Soc. Jpn. Suppl B* **2003**, *72*, 99.
(25) Takamizawa, S.; Hiroki, T.; Nakata, E.; Mochizuki, K.; Mori, W. *Chem. Lett.* **2002**, *31*, 1208.
(26) Takamizawa, S.; Nakata, E.; Yokoyama, H. *Inorg. Chem. Commun.* **2003**, *6*, 763.
(27) Kachi-Terajima, C.; Akatsuka, T.; Kohbara, M.; Takamizawa, S. *Polyhedron* **2007**, *26*, 1876.
(28) Kachi-Terajima, C.; Akatsuka, T.; Kohbara, M.; Takamizawa, S. *Chem. Asian J.* **2007**, *2*, 40.